Journal of
Manufacturing and Materials Processing

MDPI

Article

Investigation and Modeling of the Preheating Effects on Precipitation and Hot Flow Behavior for Forming High Strength AA7075 at Elevated Temperatures

Kailun Zheng [1,*], Yong Li [2], Song Yang [3], Kunning Fu [3], Jinghua Zheng [4,*], Zhubin He [1] and Shijian Yuan [1]

1 Department of Mechanical Engineering, Dalian University of Technology, Dalian 116024, China; hezb@dlut.edu.cn (Z.H.); sjyuan@dlut.edu.cn (S.Y.)
2 Department of Mechanical Engineering and Automation, Beihang University, Beijing 100191, China; liyong19@buaa.edu.cn
3 Department of Material Science and Engineering, Harbin Institute of Technology, Harbin 150001, China; yangsong@baicorv.com (S.Y.); 19B909110@stu.hit.edu.cn (K.F.)
4 Department of Mechanical Engineering, Imperial College London, London SW7 2AZ, UK
* Correspondence: zhengkailun@dlut.edu.cn (K.Z.); jinghua.zheng13@imperial.ac.uk (J.Z.)

Received: 17 June 2020; Accepted: 21 July 2020; Published: 23 July 2020

Abstract: Preheating is the first but critical step for hot stamping high strength precipitate hardened aluminum alloys. To thoroughly understand the effects of preheating conditions—i.e., preheating rate and heating temperature—on the strength and hot deformation of aluminum alloys, a series of thermal–mechanical tests was performed to determine the post-hardness evolution and hot flow behaviors. Typical microstructures with different preheating conditions were also observed through transmission electron microscopy (TEM), with which a unified model of both hot flow and strength based on key microstructural variables was developed, enabling the successful prediction of macroscopic properties using different preheating strategies. The results have shown that for high strength AA7075 at the T6 condition, the dominant mechanism of precipitate evolution with increasing temperature is the coarsening of precipitates first, followed by dissolution when they exceed a critical temperature. A higher heating rate results in a slower coarsening and a relatively higher strength level. In addition, the flow stress of hot deformation is also higher using a quick heating rate, with more significant softening and reduced ductility.

Keywords: aluminum alloy; heating rate; precipitation; flow behavior; hot forming

1. Introduction

Complex-shaped thin-walled panels of lightweight aluminum alloys are increasingly used in the body structures of automobile, aircraft and aerospace vehicles [1–4]. It is preferable to form such components by stamping at elevated temperatures to overcome the poor ductility at room temperature and springback [5]. In terms of forming processes at elevated temperatures, warm (T < 0.6 Tm, T and Tm are respectively the forming temperature and melting temperature) and hot (T > 0.6 Tm) stamping are classified depending on whether dynamic recrystallization occurs in the alloy.

For the hot stamping condition, hot form quench (HFQ®) is the cutting-edge technology used to manufacture high strength aluminum alloy components, enabling complex shapes and satisfying post-formed strength to be obtained simultaneously [6,7]. The HFQ® process is independent of the specific temper of the used alloy as forming is performed at solution heat treatment (SHT) temperature, enabling the microstructure to be stored. For the warm forming processes of non-heat-treatable aluminum alloys [8], quick plastic forming [9], patented by GM, has been widely used in AA5xxx

panels. The process uses a gas medium to replace the conventional rigid punch; however, warm forming is generally believed to be unsuitable for forming heat-treatable alloys, as the initial precipitates may become coarsened and the post-formed strength is decreased during heating and warm forming [10] and unable to obtain maximum strength. However, the warm forming of high strength heat-treatable aluminum alloys has still been extensively investigated under the premise of compromising strength requirements. Wang et al. [11] have investigated the warm deformation behavior of AA7075, and the best drawability was found to occur at a temperature near 220 °C. However, strength reduced remarkably when the forming temperature was greater than 220 °C. Huo et al. [12] also found that warm forming AA7075-T6 at 250 °C induced strength deterioration, which was caused by the coarsening of matrix precipitates. To address the disadvantage of microstructure deterioration during preheating and even forming, investigations into controlling microstructural evolution during heating by designing a proper combination of heating rate and initial alloy microstructure have been performed. Mori et al. [13] proposed a quick heating process for aircraft alloys, with which satisfactory post-formed strength of the alloys has been obtained. Zhang et al. [14] established a unified model of the complete process of directly heating aluminum alloy at the T4 condition, enabling microstructure, deformation and post-formed strength to be successfully predicted. Essentially, these studies are driven by utilizing heating rate to quickly pass the nose temperature to target forming temperature and accomplish the forming before the temperature of the material drops into sensitive zones. In order to obtain the correlation between heating rate and underlying microstructure, and to understand the subsequent hot flow and post-formed strength evolution comprehensively, quantitative research and modeling are necessary.

In this study, the effects of heating rate on the precipitation and hot behavior of high strength aluminum alloy 7075 were investigated using thermal–mechanical testing and microstructure observation. In addition, a physically based material model considering the precipitation under various heating rates was established for modeling the macro flow behavior for the first time. The mechanism of heating rate effect—i.e., the underlying correlation between micro precipitation and material flow—enables us to provide useful indications for stamping engineers to design process parameters for high strength aluminum alloys, and the developed model also facilities the improvement of simulation accuracy by considering various preheating approaches.

2. Materials and Methods

The as-received material was high strength aluminum alloy, 7075, provided by Constellium France. The initial heat treatment temper was T6. The sheet thickness was 2 mm. The main chemical composition is given in Table 1.

Table 1. The main chemical composition of 7075 in weight percentage.

Zn	Mg	Cu	Si	Fe	Mn	Cr	Ti	Al
5.1–6.1	2.1–2.9	1.2–2.0	0.4	0.5	0.3	0.18–0.28	0.2	Balanced

Figure 1 illustrates the experimentation details. A series of tensile tests under hot forming conditions with different heating rates, temperatures and strain rates were performed. Three heating rates, $\dot{T}_H$ = 0.5 °C/s, 1 °C/s and 5 °C/s, were selected to simulate the practical heating rates of the industrial heating facilities. The heating temperatures used before forming were T_H = 300 °C, 350 °C and 400 °C, ranging from warm to hot forming conditions. Once the specimen was heated to the target temperature, it was soaked for 1 s. After obtaining a uniform temperature distribution, for the heat treatment test (Test A), the specimen was immediately quenched to room temperature using the water quenching module in Gleeble. Then, the hardness was measured within the uniform temperature zone. For Test B, the specimen was hot stretched either to failure or to a certain degree of strain. Water quenching was still used to maintain the microstructure. The objective of such

intermediate quenching during hot deformation is to identify the dominant microstructure evolution. For each condition, at least three tests were performed to obtain reliable results. Figure 1b shows the used specimen. A dog-bone specimen was machined from the as-received rolled sheet using electrical discharge machining. The longitudinal direction of the specimen gauge is the rolling direction. The length and width of the parallel zone were 46 mm and 12 mm, respectively, which enables us to guarantee the 10-mm length of the uniform temperature zone using the resistance heating of the Gleeble 3800 thermo-mechanical simulator. In addition, a sufficiently large area for determining mechanical properties and statistical microstructure observations was used to prepare microstructure samples. The conducted mechanical tests are summarized in Table 2.

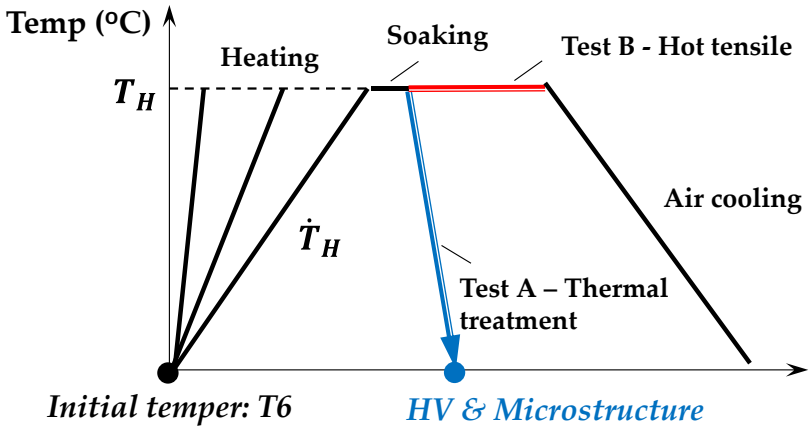

(**a**)

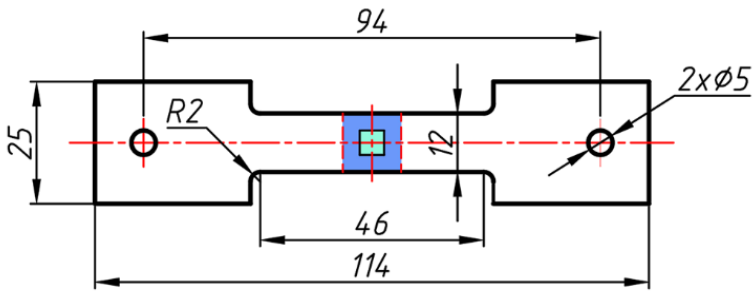

(**b**)

Figure 1. Experimentation details: (**a**) schematic of temperature profile and (**b**) specimen design (all dimensions are in mm).

Table 2. Conditions for Gleeble hot deformation and post-deformation hardness tests.

	Test Conditions		
	Heating Rate (°C/s)	**Heating Temperature (°C)**	**Strain Rate (1/s)**
Hardness test	1, 5	120, 200, 300, 350, 400, 425, 450, 485	-
Hot uniaxial tensile test	0.5, 1, 5	300, 350, 400	0.1, 1, 5

TEM and Electron backscatter diffraction (EBSD) observations were performed on typical samples under selected conditions to provide microstructure evidence (i.e., precipitates and grain sizes, respectively), aiming to validate the mechanisms in the proposed physically based constitutive

equations, where the middle heating rate of 1 °C/s was selected as the typical condition. The detailed conditions for the microstructure observations are given in Table 3. TEM tests of ①, ② and ③ were used to examine the temperature effects on the coarsening of the precipitates during heating. EBSD tests of ④, ⑤ and ⑥ were used to examine the grain size evolution after heating and after heating and straining.

Table 3. Conditions for microstructure observations.

	As-Received	As-Heated		As-Heated and Strained
		1 °C/s, 300 °C	1 °C/s, 400 °C	1 °C/s, 400 °C + ε:0.3
TEM	√①	√②	√③	
EBSD	√④		√⑤	√⑥

3. Unified Constitutive Modeling and Calibration

A unified constitutive model is proposed and calibrated in this section, so as to predict the evolutions of both key microstructures (including precipitates and solid solutes) and the mechanical properties (hardness and hot deformation behavior) of AA7075-T6 during and after heating with different heating rate conditions.

3.1. Modeling of Precipitation during Heating

It has been widely reported that precipitates are the key microstructures to determine the mechanical properties of age-hardened aluminum alloys during heat treatments. Hence, the evolutions of precipitate related parameters are modeled in this section. Figure 2 summarizes the schematic of the precipitation sequence during heating at a particular heating rate for AA7075 material from previous publications [15], from which the nucleation and dissolution temperature ranges for different precipitates can be observed.

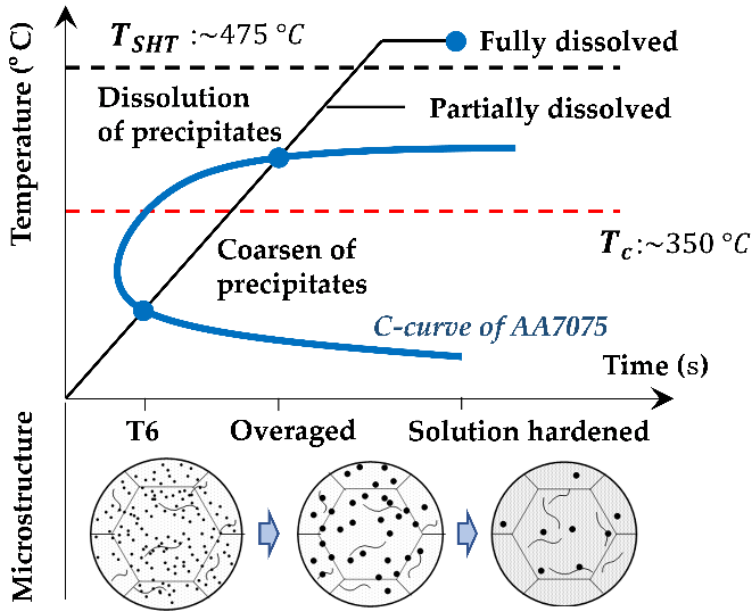

Figure 2. Schematic of precipitation sequences and kinematics during heating of AA7050 with different heating rates.

For the AA7075-T6 investigated in this study, it is generally believed that η' is the dominant precipitate for strengthening, which starts to dissolve when the temperature is high enough (between 300 to 400 °C) under different heating rates [16]. Hence, during heating, the initial η' precipitates in the T6 temper material would experience coarsening first, and then start to dissolve when being heated to above the critical temperature T_c. Both the coarsening and dissolution of precipitates are modeled here.

Coarsening of precipitates has been widely reported and modeled before; the radius data is generally used for modeling. The following equation is used to predict the coarsening of precipitates, considering the different temperature effects [17,18] as the following:

$$\dot{\bar{r}} = k_1 \exp\left(-\frac{Q_{diff}}{RT}\right)(Q - \bar{r})^{n_1} \tag{1}$$

where $\bar{r}$ is the normalized precipitate radius, which is defined as $\bar{r} = r/r_c$ (r is the precipitate radius and r_c is the critical radius at the peak ageing state). Q_{diff} is the activation energy for diffusion, R is the universal constant, Q represents the largest normalized radius of precipitates during heating, and k_1 and n_1 are material constants.

When the alloy is heated to a critical temperature T_c, the dissolution of coarsened precipitates occurs, and solid solutes will diffuse from precipitates to the matrix of the material, contributing to the strength of the material with solution hardening effects [19,20]. The evolution of solute concentration in the matrix of the material can be modeled as follows [20]:

$$\dot{\bar{c}} = \begin{cases} -k_2 \exp\left(-\frac{Q_s}{RT}\right)(\bar{c} - 1), \text{ when } T \geq T_c \\ 0, \text{ when } T < T_c \end{cases} \tag{2}$$

$\bar{c}$ is the normalized solute concentration in the matrix, Q_s is the free energy of the solution of the solute and k_2 is a material constant. The volume fraction of precipitates will change due to dissolution, whose evolution can be modeled according to the solute concentration as the following [21]:

$$\bar{f} = \frac{1 - \bar{c}}{1 - \bar{c}_e} \tag{3}$$

in which $\bar{c}_e$ is the equilibrium solute concentration at the previous ageing conditions, defined as follows [21]:

$$\bar{c}_e = exp\left[-\frac{Q_s}{R}\left(\frac{1}{T_f} - \frac{1}{T_s}\right)\right] \tag{4}$$

When the material is initially at peak aged state, the further coarsening of precipitates would lead to the over-ageing behavior of the material, and, hence, the precipitation hardening mechanism is believed to be controlled by bypassing. The strengthening contribution from the precipitates then can be modeled by the bypassing mechanism, as the following [21]:

$$\sigma_A = C_a \bar{f}^{n_2} / \bar{r}^{n_3} \tag{5}$$

Meanwhile, solid solution hardening from solid solutes can be modeled by the following [21]:

$$\sigma_{ss} = C_{ss} \bar{c}^{2/3} \tag{6}$$

The total yield strength of the material due to precipitation and solid solutes can be modeled according to the mixture law, as the following:

$$\sigma_y = \sigma_0 + \sqrt{\sigma_A^2 + \sigma_{ss}^2} \tag{7}$$

In Equations (5) to (7), C_a, C_{ss} and σ_0 are temperature-dependent material constants, which are defined as follows:

$$C_a = C_{a0}\exp(-\alpha_a T) \tag{8}$$

$$C_{ss} = C_{ss0}\exp(-\alpha_{ss} T) \tag{9}$$

$$\sigma_0 = C_{\sigma 0}\exp(-\alpha_\sigma T) \tag{10}$$

3.2. Modeling of Hot Deformation

The constitutive model for hot deformation behavior after preheating of AA7075 is proposed and introduced in this section. During deformation at high temperatures with different types of precipitates existing in the aluminum alloys, different mechanisms may occur. For example, recrystallization has been reported to occur at high temperatures and high strain levels for aluminum alloys. Meanwhile, the damage evolutions of the alloy may also be affected by the precipitation states. A physical mechanism-based viscoplastic model is proposed in this section for aluminum alloys under hot stamping conditions (heating rate, temperature and strain rate) from [22,23], and the dominant equations are given as follows.

$$\dot{\varepsilon}_p = \frac{\sigma/(1-\omega) - \sigma_d - \sigma_y}{K}^{n} \overline{d}^{-\gamma_1} \tag{11}$$

$$\sigma_d = B\sqrt{\overline{\rho}} \tag{12}$$

$$\dot{\overline{\rho}} = A(1-\overline{\rho})\left|\dot{\varepsilon}_p\right| - C_1\overline{\rho}^{m_1} - \left(\frac{C_2\overline{\rho}}{1-S}\right)\dot{S} \tag{13}$$

$$\dot{S} = \frac{q_1(0.1+S)^{m_2}(1-S)\overline{\rho}^2}{\overline{d}} \tag{14}$$

$$\overline{\rho}_c = q_2\dot{\varepsilon}^4 \tag{15}$$

$$\dot{\overline{d}} = G_1\overline{d}^{m_3} - G_2\dot{S}\overline{d}^{m_4} \tag{16}$$

$$\dot{\omega} = \frac{1}{\left(\overline{r}\overline{f}\right)^{m_5}}\frac{\eta_1}{(1-\omega)^{\eta_3}}\left(\sigma\dot{\varepsilon}_p\right)^{\eta_2} \tag{17}$$

$$\sigma = E(1-\omega)\left(\varepsilon - \varepsilon_p\right) \tag{18}$$

The viscoplastic behavior of alloys under hot deformation conditions is described by Equation (11), in which $\dot{\varepsilon}_p$ is the plastic strain rate, σ is the flow stress and σ_y is the yield stress of the material. The particular yield stress data with different heating conditions can be determined using Equation (7). The dislocation hardening component σ_d is modeled according to a normalized dislocation density, $\overline{\rho}$, which is defined as $\overline{\rho} = (\rho - \rho_i)/\rho_{max}$. ρ_i and ρ_{max} are the initial and maximum dislocation density of the material, respectively, and $\overline{\rho}$ then can be set as varying from 0 to 1, when considering that $\rho_i \ll \rho_{max}$. $\overline{\rho}$ during hot deformation is modeled by Equation (13), in which the accumulation and dynamic recovery of dislocations caused by plastic straining is represented by the first term of the equation, the static recovery effect is then described by the second term [23], and, in addition, the possible recrystallization effect on the dislocation evolution has been modeled by the third term in Equation (13).

Dynamic recrystallization is directly related to the dislocation density, and when $\overline{\rho}$ reaches a critical level with the proceeding of straining, dynamic recrystallization may occur. The recrystallization model considering the dislocation density and grain size effect proposed by [24,25] is used in this study, as given in Equation (14). The critical level of $\overline{\rho}$ for recrystallization ($\overline{\rho}_c$) is defined in Equation (15). Meanwhile, a kinematic grain size model considering the effects of grain growth and dynamic recrystallization has been used and is given in Equation (16).

A damage factor ω for characterizing the damage evolution during hot deformation is defined in Equation (17). The effect of precipitation of the damage evolution at an over-aged condition has been considered in Equation (17) by the term of $1/\left(\overline{rf}\right)^{m_5}$. It is assumed that failure occurs when the damage factor reaches 0.7. Equation (18) is the hook's law, in which the damage factor effect on the decrease in flow stress is introduced.

In the above equations, a number of material parameters are temperature-dependent. The Arrhenius equation is used to model these temperature-dependent parameters, as below:

$$K = K_0 \exp\left(\frac{Q_K}{RT}\right) \tag{19}$$

$$n = N_0 \exp\left(\frac{Q_n}{RT}\right) \tag{20}$$

$$B = B_0 \exp\left(\frac{Q_B}{RT}\right) \tag{21}$$

$$A = A_0 \exp\left(\frac{Q_A}{RT}\right) \tag{22}$$

$$C_1 = C_{10} \exp\left(\frac{Q_{C_1}}{RT}\right) \tag{23}$$

$$C_{ss1} = C_{ss10} \exp\left(\frac{Q_{C_{ss1}}}{RT}\right) \tag{24}$$

$$\eta_1 = \eta_{10} \exp\left(-\frac{Q_{\eta_1}}{RT}\right) \tag{25}$$

$$\eta_2 = \eta_{20} \exp\left(\frac{Q_{\eta_2}}{RT}\right) \tag{26}$$

$$\eta_3 = \eta_{30} \exp\left(-\frac{Q_{\eta_3}}{RT}\right) \tag{27}$$

$$E = E_0 \exp\left(\frac{Q_E}{RT}\right) \tag{28}$$

$$G_1 = G_{10} \exp\left(\frac{Q_{G_1}}{RT}\right) \tag{29}$$

$$q_2 = q_{20} \exp\left(\frac{Q_{q_2}}{RT}\right) \tag{30}$$

3.3. Modeling Calibration

Most of the equations developed above are non-linear ordinary differential equations, which cannot be solved analytically. Some material constants (such as Q_{diff} and Q_s) have particular physical meanings and have been obtained in previous studies, while other material constants need to be calibrated according to the experimental results obtained in Section 2. An evolutionary algorithm optimization method to obtain the minimum sum of the squares of errors between experiments and numerical data, which has been detailed in [26,27], has been used for the calibration process in order to achieve the optimized material constants in this study. The experimental data of hardness results were used to calibrate the material constants in the yield strength equations, while the hot flow behavior results from Section 2 were used to calibrate the material constants in the hot deformation equations above. It should be noted that the determined hot uniaxial tensile results were used, which has been extensively used for model calibration [5,7,28] and is believed to be able to investigate the effects of hot stamping conditions (heating rate, temperature and strain rate). The objective function of the

evolutionary optimization method is defined by experimental and numerical differences of hardness or flow behavior at the same testing condition. The more detailed functions and algorithms can be referred to in previous studies [26,27].

The material constants in the developed equations for the heating and hot deformation stages are calibrated according to the results shown in Section 4 and are listed in Tables 4 and 5, respectively.

Table 4. Material constants in the developed model for heating and hardness.

k_1 (-)	n_1 (-)	Q (-)	Q_{diff} (kJ/mol)	k_2 (-)	Q_s (kJ/mol)	C_{a0} (MPa)
1.2×10^4	1.5	6.0	76.5	4.5×10^{-1}	32.0	968.1
α_a (kJ/mol)	C_{ss0} (MPa)	α_{ss} (MPa)	$C_{\sigma 0}$ (MPa)	$\alpha_{\sigma 0}$ (-)	n_2 (-)	n_3 (-)
2.6×10^{-3}	452.7	2.2×10^{-3}	304.7	4.6×10^{-3}	0.1	0.8

Table 5. Material constants in the developed model for hot deformation.

m_1 (-)	K_0 (MPa)	Q_K (J/mol)	N_0 (-)	Q_n (J/mol)	B_0 (MPa)	Q_B (J/mol)	A_0 (-)	Q_A (J/mol)	C_{10} (s^{-1})
0.3	0.236	23,368	−0.37	11,567	0.0036	48,322	18.21	4093.3	2784
Q_{C_1} (J/mol)	C_2 (-)	q_1 (s^{-1})	m_2 (-)	q_{20} (MPa)	Q_{q_2} (J/mol)	G_{10} (s^{-1})	Q_{G_1} (J/mol)	G_2 (-)	m_3 (-)
29,514	0.1	60.0	1.1	1.7×10^{-7}	58,716	1.4×10^{-5}	41,173	1.5	0.97
m_4 (-)	m_5 (-)	η_{10} (-)	Q_{η_1} (J/mol)	η_{20} (-)	Q_{η_2} (J/mol)	η_{30} (-)	Q_{η_3} (J/mol)	E_0 (MPa)	Q_E (J/mol)
0.58	−0.01	2.55×10^{-2}	20,959	0.57	20,470	2.05	3776.3	3369	12,596

4. Results and Discussions

In this section, to facilitate the understanding of precipitation and grain evolution during heating and hot straining, and to obtain quantitative data for modeling, TEM and EBSD observations were performed in order to identify the key microstructures, including grains and precipitates.

4.1. Microstructure Evolution

Figure 3 shows the TEM photos of the precipitate evolutions of AA7075 heated to different temperatures with a rate of 1 °C/s. Compared to the fine and dense distributed precipitates, η′, in the as-received T6 condition, an obvious coarsening of precipitates can be observed once the material is heated to 300 °C. such coarsened precipitates is believed to indicate the over-aged state. With further heating of the material, as illustrated in Figure 2, once the temperature becomes greater than the critical temperature, $T > T_c$, the previously coarsened precipitates begin to dissolve into the matrix again. The size of precipitates is reduced for the heated temperature of 350 °C, as shown in the Figure 3c. The results correspond well to the proposed mechanism in Figure 2. The critical temperature depends on various factors: for the preheating conditions investigated in this study, both initial temper and heating rate could affect the critical temperature. In general, a higher heating rate would lead to a higher T_c [19]. The obtained precipitates under different conditions would result in different hot flow behavior and post-strength if the final forming temperature is lower than the SHT temperature. The coarsened precipitates inevitably occupied useful elements for post artificial ageing, resulting in sacrificed strength under warm forming conditions. In terms of the advanced HFQ® process, the effect of heating rate is believed to be weakened as the material experiences a full solution heat treatment. For different heating rates, the precipitate behavior is expected to be similar, with precipitates coarsened first and then dissolved depending on the critical dissolution temperatures, which has been reported using the differential scanning calorimetry (DSC) measures in quite a few studies [29,30]. Hence, we only performed TEM for a single heat rate in order to provide indications of this behavior in this study and support the development of the microstructure-based constitutive model in the following sections.

Figure 4 shows the EBSD maps of the samples before heating, after heating and after heating and hot straining to demonstrate the grain evolution during the investigated process. Misorientations > 15° are identified as grain boundaries (black lines in Figure 4). As seen in Figure 4a, coarse grains, ranging

from 50 to 100 μm, were presented in the as-received sample, where some small grains with a size of ~20 μm were also observed. Heating the sample to 400 °C using a rate of 1 °C/s did not significantly affect the grain sizes, where coarse grains were still present, as shown in Figure 4b. However, after the hot deformation to a true strain level of 0.3, an apparent grain size reduction was observed, as in Figure 4c. This is evidenced by the increased amount of small grains in the deformed samples, indicating the occurrence of dynamic recrystallization. Such microstructure observation is also consistent with the findings in [31], confirming the reliability of our results.

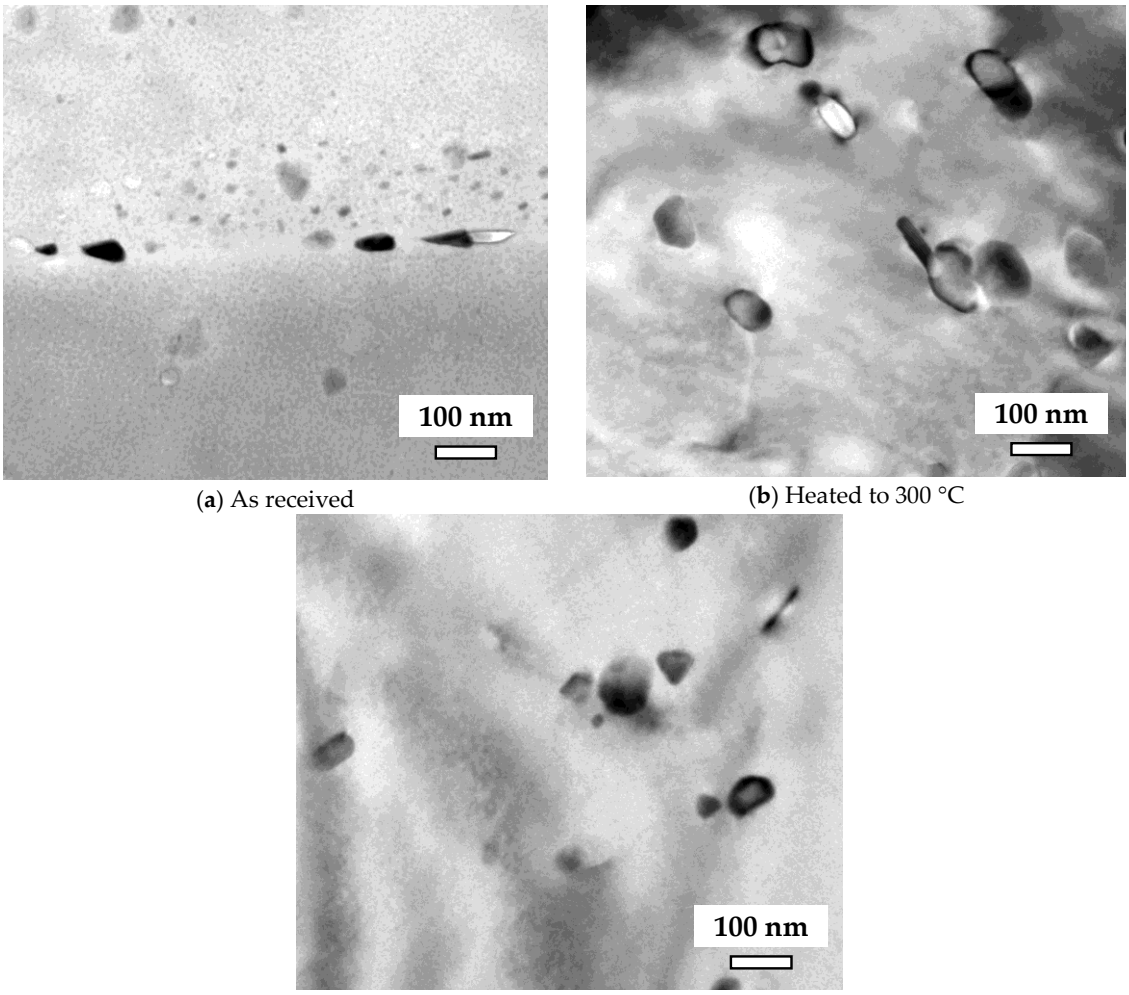

(**a**) As received (**b**) Heated to 300 °C

(**c**) 350 °C

Figure 3. Typical TEM observations on the quenched samples that were heated to different temperatures using a heating rate of 1 °C/s. (**a**) As-received, (**b**) heated to 300 °C and (**c**) heated to 350 °C.

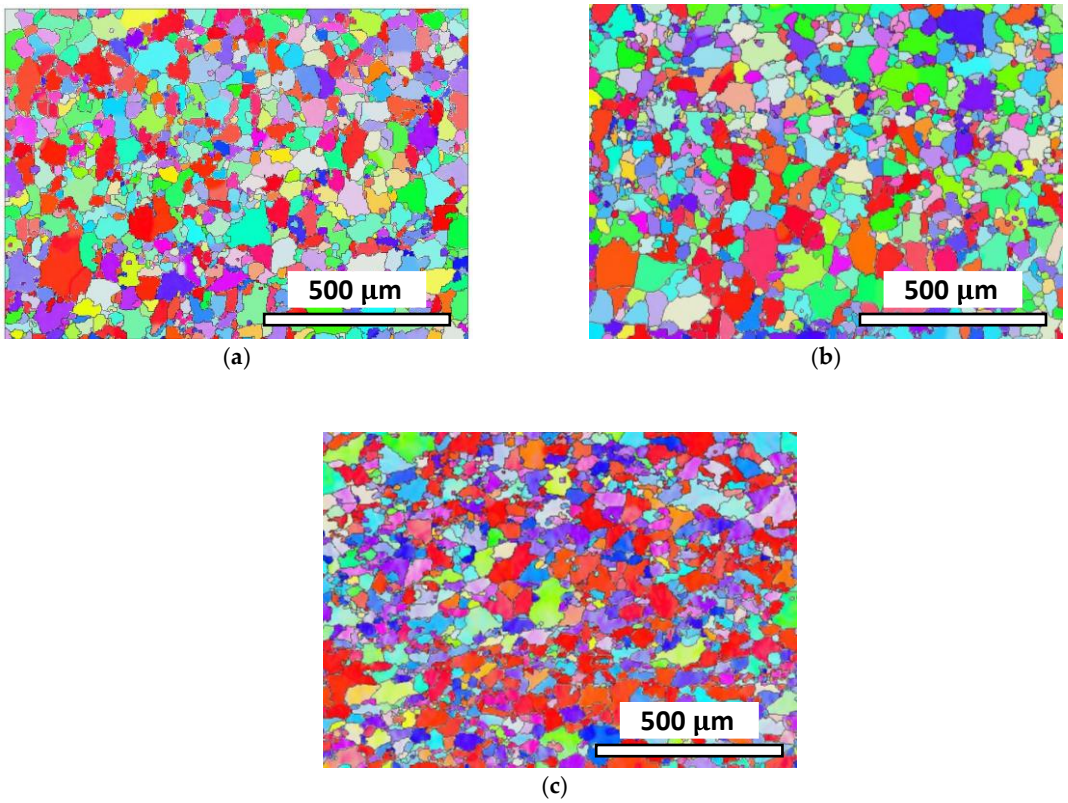

Figure 4. EBSD observations of (**a**) the as-received T6 sample, (**b**) the sample heated to 400 °C and (**c**) post hot tensile to a total strain of 0.3 at 400 °C.

4.2. Effects of Preheating on Strength

As reasoned in Figure 2, preheating—i.e., heating rate and heated temperature—would result in varied precipitation in the matrix, which exhibits the varied post-formed strength of the material. Figure 5 shows the effects of heating rate on the strength of AA7075 for a series of heated temperatures.

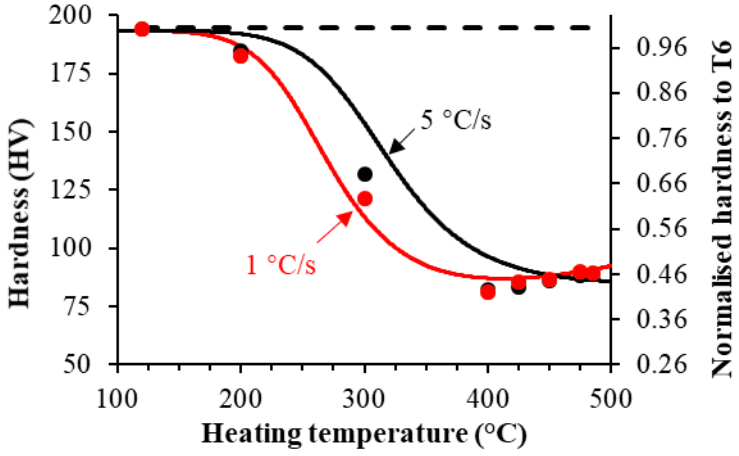

Figure 5. Effect of heating rate on hardness of AA7075-T6 heated to different temperatures, where the symbols represent the experimental determined hardness and the solid lines represent the model predictions.

In order to suppress the natural ageing effect, hardness was used instead of yield strength for a quick manual manipulation. Two heating rates, 1 °C/s and 5 °C/s, were compared. As can be seen

in this figure, for both heating rates, the hardness drops initially, which is believed to be caused by the coarsening of precipitates (η′). Compared to the as-received T6 condition, the microstructure is similar to an over-aged state, resulting in the reduced strength. When the temperature is higher than 400 °C, the hardness level starts to increase as the dissolution of coarsened precipitates occurs, and solid solution hardening contributes to this. Compared the hardness levels of both heating rates, initially, hardness using 1 °C/s is lower than that of 5 °C/s. The reason is believed to be that, for a higher heating rate, the relative soaking time is short and the coarsening of precipitates is not severe. Meanwhile, when the temperature is higher than 400 °C, a slower heating rate would result in a longer heating time, which contributes to the dissolution of more precipitates, and the resulted solid solution hardening is enhanced, which results in the reversion of hardness levels. The comparisons between experimental results (symbols) and model predictions (solid lines) are also shown in Figure 5, where symbols represent the experimental determined hardness and the solid lines represent the model predictions. Both the above-mentioned hardness evolutions can be predicted excellently using the established model.

Figure 6 shows the modeling results of the microstructures during heating of the alloy using heating rates of 0.1, 1 and 5 °C/s. In general, before the temperature of 400 °C, the coarsening of precipitates occurs during heating, and a higher coarsening speed is observed with a lower heating rate. Dissolution occurs when the heated temperatures reach a critical value, which has been predicted in Figure 6b (T_c is defined as 350 °C in this study [19]). Solute concentration starts to increase due to the dissolution that occurs with the decreasing volume fraction of precipitates. In addition, a comparatively higher critical temperature is predicted with higher heating rates, as shown in Figure 6b, which corresponds well with the findings in previous publications.

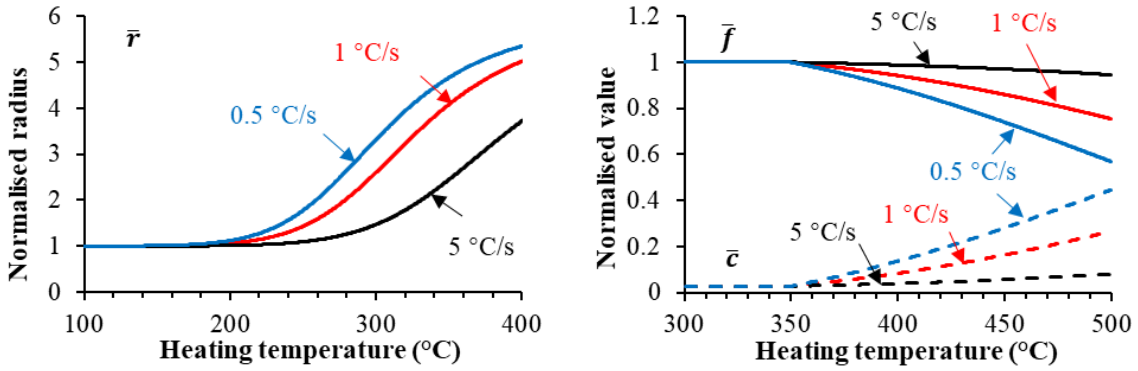

(**a**) Precipitate radius (**b**) Volume fraction and solute concentration

Figure 6. Modeling results of evolution of key microstructures during heating of AA7075-T6 with indicated heating rates: (**a**) precipitate radius and (**b**) volume fraction and solute concentration.

4.3. Effects of Preheating on Hot Flow Behavior

Figure 7 shows the effects of preheating on the hot flow behavior for different temperatures using three different heating rates, 0.5, 1, and 5 °C/s, where the solid symbols represent the experimental results and the solid lines are the model predictions. The used strain rate was 1/s. Good predictions were achieved as both the flow stress level and ductility could be precisely predicted. For the stress–strain curves at 350 °C shown in Figure 7a, the flow stress level of 5 °C/s is the highest among the three heating rates, while those of the other two rates are similar. Such a finding is consistent with that of hardness variation in Figure 5. During heating to 350 °C, the coarsening of precipitates occurs, in which that of 5 °C/s is the smallest, resulting in the highest flow stress level. In addition, for all three rates, an obvious softening of flow stress can be observed, which is believed to be caused by the occurrence of dynamic recrystallisation and microdamage around precipitates. During stretching, precipitates are hard particles, and microcracks are easy to initiate at the boundaries due to the incompatible deformation between precipitates and matrix. For the strain to failure, the slower the

heating rate, the greater the ductility; the reason for this is that microcracks may initiate around the precipitates during stretching. The denser the precipitates distributed, the higher the probability of damage, and, subsequently, the ductility becomes lower. With further heating of the material to 400 °C, the previously coarsened precipitates begin to dissolve; a quicker heating rate induces a relatively shorter soaking time. Therefore, the flow stress level of 5 °C/s is still the highest, as the solid solution hardening is limited. The flow stress levels of 1 and 0.5 °C/s are similar as the coarsened precipitates might be dissolved to a similar extent at such a high temperature.

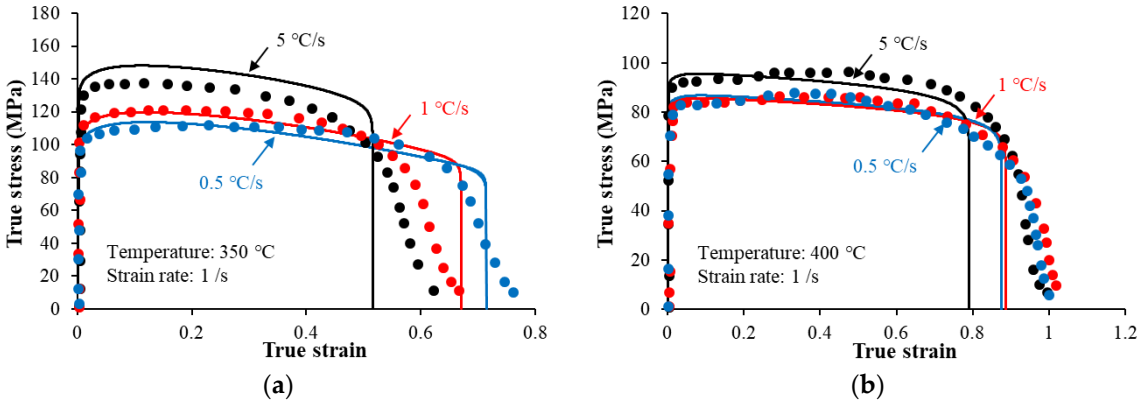

Figure 7. True stress and strain curves of AA7075-T6 heated to (**a**) 350 °C and (**b**) 400 °C with different heating rates under strain rate of 1/s (experimental results: symbols; modeling results: lines).

4.4. Model Verification

To further verify the robustness of this model, hot flow behaviors at a variety of temperatures and strain rates were predicted and compared to the experimental results (solid symbols). As shown in Figure 8a, the flow stress level, ductility and softening can be accurately predicted. The severest softening is observed for the curve at the temperature of 300 °C; this is assumed to be caused by damage around precipitates, as dynamic recrystallisation is unable to occur at this temperature. For different strain rates at the temperature of 400 °C, obvious hardening is observed, as both strain and strain rate hardening cooperatively functioned. The quick heating rate results in higher density of accumulated dislocation and a shorter time of recovery. The flow behavior is believed to be the mutual effect of dislocation accumulation, recovery and recrystallisation. Meanwhile, for the lowest strain rate, 0.1/s, a gentle increase in flow stress is observed, which might be caused by the grain growth. For the middle strain rate, 1/s, the severest softening is found as the dynamic recrystallisation dominates.

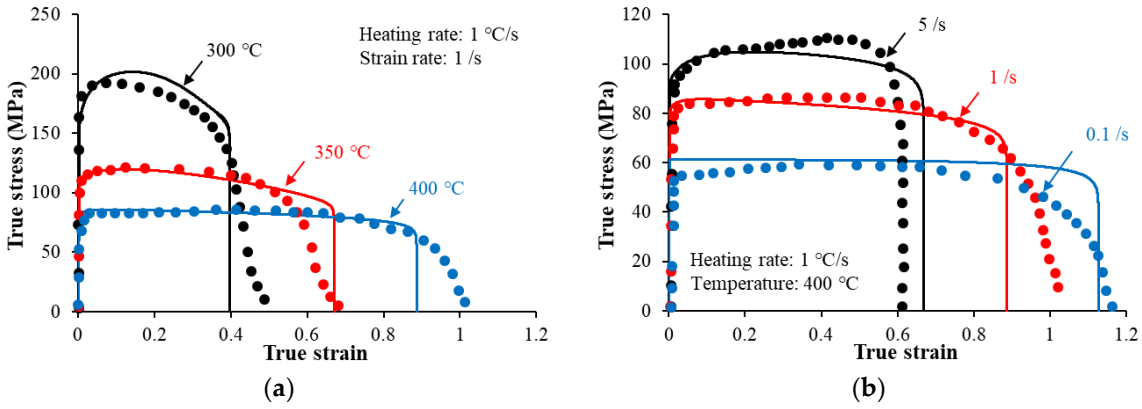

Figure 8. True stress and strain curves of AA7075-T6 heated to (**a**) different temperatures with heating rate of 1/s and (**b**) 400 °C with different strain rates (experimental results: symbols; modeling results: lines).

5. Conclusions

An advanced, physically based, constitutive model, incorporating microstructure evolutions as the key variables, has been developed in this work, based on an experimental investigation of the hot flow behavior of AA7050. The main conclusions drawn are indicated below:

(1) The precipitate coarsening and dissolution of AA7050-T6 during heating were considered in the unified constitutive model, enabling appropriate predictions of the heating rate effects on both the strength and hot flow behaviors of the alloy.

(2) Increasing the target heating temperature leads to a rapid reduction in the post-forming hardness followed by a slight increase, due to the coarsening and subsequent dissolution of the precipitates. A higher heating rate results in delayed hardness reduction due to the shortened heating time.

(3) An increase in the heating rate from 0.5 °C/s to 5 °C/s increased the flow stress levels, from 100 MPa to 130 MPa at 350 °C and from 80 to 90 MPa at 400 °C. This is attributed to the coarsening of the precipitates during heating prior to the deformation.

Author Contributions: Conceptualization, K.Z. and S.Y. (Shijian Yuan); methodology, K.Z. and J.Z.; modeling and validation, K.Z., Y.L. and K.F.; formal analysis, K.Z., Y.L. and J.Z.; writing—original draft preparation, K.Z., Y.L., S.Y. (Song Yang) and Z.H.; writing—review and editing, K.Z. and Y.L.; supervision, S.Y. (Shijian Yuan). All authors have read and agreed to the published version of the manuscript.

Funding: The research in this paper was funded by the European Union's Horizon 2020 research and innovation program (Grant No. 723517) as part of the project "Low Cost Materials Processing Technologies for Mass Production of Lightweight Vehicles (LoCoMaTech)". The authors would also like to thank the LiaoNing Revitalization Talents Program (XLYC 1802065) for its support.

Acknowledgments: The authors would like to express gratitude to Jianguo Lin from Imperial College London for the supervision and help with the research. The authors would like to express sincere thanks to Fenggong Lv, Yujie Han and Haitao Qu from Avic Manufacturing Technology Institute for their great support of the microstructure observation in this study.

Conflicts of Interest: The authors declare no conflict of interest.

References

1. Zheng, K.; Politis, D.; Wang, L.; Lin, J. A review on forming techniques for manufacturing lightweight complex—Shaped aluminium panel components. *Int. J. Light. Mater. Manuf.* **2018**, *1*, 55–80. [CrossRef]
2. Zheng, K.; Lee, J.; Xiao, W.; Wang, B.; Lin, J. Experimental Investigations of the In-Die Quenching Efficiency and Die Surface Temperature of Hot Stamping Aluminium Alloys. *Metals* **2018**, *8*, 231. [CrossRef]
3. Hirsch, J.; Hirsch, J. Recent development in aluminium for automotive applications. *Trans. Nonferrous Met. Soc. China* **2014**, *24*, 1995–2002. [CrossRef]
4. Palumbo, G.; Piccininni, A.; Guglielmi, P.; Spina, R.; Tricarico, L.; Sorgente, D.; Russello, G.; Vitrano, A.; Franco, A.L. Warm Forming of an AA5754 Component for Railway Vehicle Applications. *Procedia Eng.* **2017**, *183*, 351–356. [CrossRef]
5. Mohamed, M.S.; Foster, A.D.; Lin, J.; Balint, D.S.; Dean, T.A. Investigation of deformation and failure features in hot stamping of AA6082: Experimentation and modelling. *Int. J. Mach. Tools Manuf.* **2012**, *53*, 27–38. [CrossRef]
6. Zheng, K.; Dong, Y.; Zheng, J.-H.; Foster, A.; Lin, J.; Dong, H.; Dean, T.A. The effect of hot form quench (HFQ®) conditions on precipitation and mechanical properties of aluminium alloys. *Mater. Sci. Eng. A* **2019**, *761*, 138017. [CrossRef]
7. El Fakir, O.; Wang, L.; Balint, D.; Dear, J.P.; Lin, J.; Dean, T.A. Numerical study of the solution heat treatment, forming, and in-die quenching (HFQ) process on AA5754. *Int. J. Mach. Tools Manuf.* **2014**, *87*, 39–48. [CrossRef]
8. Toros, S.; Ozturk, F.; Kacar, I. Review of warm forming of aluminum–magnesium alloys. *J. Mater. Process. Technol.* **2008**, *207*, 1–12. [CrossRef]
9. Krajewski, P.E.; Schroth, J.G. Overview of quick plastic forming technology. *Mater. Sci. Forum* **2007**, *551*, 3–12. [CrossRef]

10. Zheng, K.; Dong, Y.; Zheng, D.; Lin, J.; Dean, T.A. An experimental investigation on the deformation and post-formed strength of heat-treatable aluminium alloys using different elevated temperature forming processes. *J. Mater. Process. Technol.* **2019**, *268*, 87–96. [CrossRef]
11. Wang, H.; Luo, Y.; Friedman, P.; Chen, M.-H.; Gao, L. Warm forming behavior of high strength aluminum alloy AA7075. *Trans. Nonferrous Met. Soc. China* **2012**, *22*, 1–7. [CrossRef]
12. Huo, W.; Hou, L.; Zhang, Y.; Zhang, J. Warm formability and post-forming microstructure/property of high-strength AA 7075-T6 Al alloy. *Mater. Sci. Eng. A* **2016**, *675*, 44–54. [CrossRef]
13. Maeno, T.; Mori, K.-I.; Yachi, R. Hot stamping of high-strength aluminium alloy aircraft parts using quick heating. *CIRP Ann.* **2017**, *66*, 269–272. [CrossRef]
14. Zhang, Q.; Luan, X.; Dhawan, S.; Politis, D.J.; Du, Q.; Fu, M.; Wang, K.; Gharbi, M.M.; Wang, L. Development of the post-form strength prediction model for a high-strength 6xxx aluminium alloy with pre-existing precipitates and residual dislocations. *Int. J. Plast.* **2019**, *119*, 230–248. [CrossRef]
15. Priya, P.; Johnson, D.R.; Krane, M.J. Precipitation during cooling of 7XXX aluminum alloys. *Comput. Mater. Sci.* **2017**, *139*, 273–284. [CrossRef]
16. Lloyd, D.J.; Chaturvedi, M.C. A calorimetric study of aluminium alloy AA-7075. *J. Mater. Sci.* **1982**, *17*, 1819–1824. [CrossRef]
17. Nicolas, M.; Deschamps, A. Characterisation and modelling of precipitate evolution in an Al–Zn–Mg alloy during non-isothermal heat treatments. *Acta Mater.* **2003**, *51*, 6077–6094. [CrossRef]
18. Zheng, J.-H.; Lin, J.; Lee, J.; Pan, R.; Li, C.; Davies, C.M. A novel constitutive model for multi-step stress relaxation ageing of a pre-strained 7xxx series alloy. *Int. J. Plast.* **2018**, *106*, 31–47. [CrossRef]
19. Milkereit, B.; Schick, C.; Keßler, O.; Osten, J. Dissolution and precipitation behaviour during continuous heating of Al–Mg–Si Alloys in a wide range of heating rates. *Materials* **2015**, *8*, 2830–2848. [CrossRef]
20. Li, Y.; Shi, Z.; Lin, J.; Yang, Y.-L.; Rong, Q.; Huang, B.-M.; Chung, T.-F.; Tsao, C.-S.; Yang, J.-R.; Balint, D.S. A unified constitutive model for asymmetric tension and compression creep-ageing behaviour of naturally aged Al-Cu-Li alloy. *Int. J. Plast.* **2017**, *89*, 130–149. [CrossRef]
21. Shercliff, H.; Ashby, M. A process model for age hardening of aluminium alloys—I. The model. *Acta Met. Mater.* **1990**, *38*, 1789–1802. [CrossRef]
22. Lin, J.; Dean, T. Modelling of microstructure evolution in hot forming using unified constitutive equations. *J. Mater. Process. Technol.* **2005**, *167*, 354–362. [CrossRef]
23. Lin, J. A set of unified constitutive equations for modelling microstructure evolution in hot deformation. *J. Mater. Process. Technol.* **2003**, *143*, 281–285. [CrossRef]
24. Ji, H.; Liu, J.; Wang, B.; Tang, X.; Lin, J.; Huo, Y. Microstructure evolution and constitutive equations for the high-temperature deformation of 5Cr21Mn9Ni4N heat-resistant steel. *J. Alloys Compd.* **2017**, *693*, 674–687. [CrossRef]
25. Alabort, E.; Putman, D.; Reed, R. Superplasticity in Ti–6Al–4V: Characterisation, modelling and applications. *Acta Mater.* **2015**, *95*, 428–442. [CrossRef]
26. Lin, J.; Yang, J. GA-based multiple objective optimisation for determining viscoplastic constitutive equations for superplastic alloys. *Int. J. Plast.* **1999**, *15*, 1181–1196. [CrossRef]
27. Cao, J.; Lin, J. A study on formulation of objective functions for determining material models. *Int. J. Mech. Sci.* **2008**, *50*, 193–204. [CrossRef]
28. Li, N.; Sun, C.; Guo, N.; Mohamed, M.; Lin, J.; Matsumoto, T.; Liu, C. Experimental investigation of boron steel at hot stamping conditions. *J. Mater. Process. Technol.* **2016**, *228*, 2–10. [CrossRef]
29. Li, G.-F.; Zhang, X.; Li, P.-H.; You, J.-H. Effects of retrogression heating rate on microstructures and mechanical properties of aluminum alloy 7050. *Trans. Nonferrous Met. Soc. China* **2010**, *20*, 935–941. [CrossRef]
30. Buha, J.; Lumley, R.; Crosky, A. Secondary ageing in an aluminium alloy 7050. *Mater. Sci. Eng. A* **2008**, *492*, 1–10. [CrossRef]
31. Xiao, W.; Wang, B.; Wu, Y.; Yang, X. Constitutive modeling of flow behavior and microstructure evolution of AA7075 in hot tensile deformation. *Mater. Sci. Eng. A* **2018**, *712*, 704–713. [CrossRef]